DEUTSCHES ELEKTRONEN-SYNCHROTRON DESY

DESY SR-83-15
October 1983

# CONTRAST INVESTIGATIONS OF SURFACE ACOUSTIC WAVES BY STROBOSCOPIC TOPOGRAPHY I. ORIENTATION CONTRAST

by

H. Cerva and W. Graeff

*Hamburger Synchrotronstrahlungslabor HASYLAB at DESY*



ISSN 0723-7979

NOTKESTRASSE 85 · 2 HAMBURG 52

To be sure that your preprints are promptly included in the HIGH ENERGY PHYSICS INDEX, send them to the following address ( if possible by air mail ):

DESY
Bibliothek
Notkestrasse 85
2 Hamburg 52
Germany

DESY SR-83-15
October 1983

ISSN 0723-7979

# CONTRAST INVESTIGATIONS OF SURFACE ACOUSTIC WAVES BY STROBOSCOPIC TOPOGRAPHY I. ORIENTATION CONTRAST



H. Cerva (a)
W. Graeff

Hamburger Synchrotronstrahlungslabor HASYLAB
at
Deutsches Elektronensynchrotron DESY
2000 Hamburg 52, Germany.

(a) on leave from
Institut für Angewandte und Technische Physik
Technische Universität Wien
1040 Wien, Austria.

submitted to phys. stat. sol. (a)

ISSN 0723-7979

ABSTRACT

Surface acoustic waves have been investigated by stroboscopic topography using synchrotron radiation from the storage ring DORIS. The observed contrast of the acoustic displacements of the lattice planes has the same period as the acoustic wave. It is demonstrated that the major part of the contrast is due to orientation contrast of the curved net planes. Intensity maxima correspond to valleys of the acoustic wave, minima to hills. A numerical treatment yielding ray tracing maps, intensity curves as well as focusing conditions which are in quantitative agreement with the experimental data is presented.

Akustische Oberflächenwellen wurden mittels stroboskopischer Röntgentopographie untersucht. Dazu wurde die Synchrotronstrahlung des Speicherrings DORIS benutzt. Der beobachtete Kontrast, der durch die akustische Verschiebung der Netzebenen entsteht, hat die gleiche Periodizität wie die akustische Welle. Es wurde gezeigt, daß der Hauptanteil des Kontrastes durch Orientierungskontrast der deformierten Netzebenen zustande kommt. Die Intensitätsmaxima entsprechen den Tälern der Oberflächenwelle, die Minima den Bergen. Eine numerische Behandlung ermöglicht die Berechnung der Strahlwege und damit die Simulation des Kontrastes. Außerdem erhält man einen Ausdruck für den Intensitätsverlauf und Fokussierungsbedingungen, die mit den experimentellen Ergebnissen quantitativ übereinstimmen. -

Classification:

7.; 14.4.1; 22.8.1



## 1. INTRODUCTION

Over the last two years X-ray topography experiments using a stroboscopic technique have been performed in the MHz region using the time structure of synchrotron radiation. C.-C. Glüer et al. [1] studied standing bulk waves and their effect on the image formation of dislocations in quartz. R.W. Whatmore et al. [2,3] made use of this new method when imaging travelling surface acoustic waves (SAW) on a $LiNbO_3$ television IF filter. At present the scanning electron microscope (SEM) working in the stroboscopic voltage contrast mode as introduced by H.P. Feuerbaum et al. [4,5] is the most important tool to control SAW device performance.

Though travelling waves can be visualized in the SEM no information concerning crystallographic defects and strains in the substrate can be obtained. Stroboscopic X-ray topography , however, permits to image the surface waves, crystal defects and mechanical deformations simultaneously.

From our investigations on a similar $LiNbO_3$ device we found that the characteristics of the wave contrast formation need explanation first. Then it is evident which conditions and effects should be noticed to make quantitative statements on surface wave propagation and its interaction with crystal properties.

## 2. THE STROBOSCOPIC TECHNIQUE.

Synchrotron radiation from storage rings has a very pronounced time structure as the circulating particles (electrons or positrons) are concentrated in so called bunches. Two parameters of this time structure are fixed and one can assume certain predefined values. The fixed parameters are circulation time of an individual bunch and its length, in case of DORIS 960 nsec and 150 psec, respectively. The variable parameter is the number N of stored bunches which at DORIS can vary between 1 and 480 with the restriction that 480/N is an integer. Hence the pulse repetition time varies between 2 nsec (N=480) and 960 nsec (N=1).

Most of our experiments have been performed with the storage ring running in single bunch mode which offers the greatest flexibility for

stroboscopic topography as phenomena of n times the source frequency can be investigated.

The key to stroboscopic topography is the exact synchronization of the observed process, here surface acoustic waves, to the time structure of the source. The latter is defined by a master oscillator which controls the HF-cavities of the storage ring (see Figure 1). From this oscillator a bunch trigger signal is derived to phaselock a frequency syntheziser via its external clock input to 1.040968 MHz, the frequency of a reference bunch. The frequency syntheziser can produce multiples of this fundamental frequency up to 1 GHz. A subsequent broad band amplifier delivers the driving signal for the sample up to 15 Volts amplitude. A variable delay allows for changing the phase relation between the bunch trigger and the actual photon pulse arrival in steps of 2 nsec.

As the typical exposure time in our experiments was about 1 sec, purely periodic processes can be imaged by this technique with time resolution of the order of nsecs but any irreversible phenomenon ocurring on a time scale shorter than the exposure time will obviously not be visible.

## 3. RAYLEIGH WAVES ON LITHIUM NIOBATE

Surface acoustic waves are elastic waves propagating on the surface of a solid or liquid medium (e.g. Rayleigh waves) [6]. For SAW applications this medium is a piezoelectric, anisotropic crystal. By means of an interdigital transducer (IDT) - an array of conducting strips deposited on the crystal surface - electromagnetic signals generate surface waves due to the inverse piezoelectric effect (Figure 2).

The linear theory of elasticity permits to describe elastic waves in a charge-free piezoelectric solid. These waves are found by solving a system of four coupled wave equations for the three elastic displacements $u_j$ and the electric potential $\varphi$. At large depth of the crystal $u_j$ and $\varphi$ should vanish. At the surface which we assume not to be metallized the potential should be continuous and fulfill Laplace's equation outside the crystal. Usually the solution for SAW is written as a linear combination of partial waves

$$u_j = \{\sum C^{(n)} a_j^{(n)} \exp(iKb^{(n)}x_3)\}\exp[iK(x_1-vt)] \quad j=1,2,3$$
$$\varphi = \{\sum C^{(n)} a_4^{(n)} \exp(iKb^{(n)}x_3)\}\exp[iK(x_1-vt)] \qquad (1)$$

where K is the acoustic wave number, v the phase velocity, $C^{(n)}$ the weighing coefficients, $a_j^{(n)}$ the amplitudes and $b^{(n)}$ the decay constants of the



partial waves. The geometry is explained in Figure 3. A procedure how to find the solution is outlined in [6].

The motion of an individual atom in an arbitrary SAW is elliptical. At the surface the elliptical motion is retrograde and changes its sense of circulation deeper in the substrate.

For Y-cut, Z-propagating $LiNbO_3$ (trigonal 3m, space group R3c) the wave equations decouple and only the components $u_1$, $u_3$ and $\varphi$ form the SAW. The component $u_2$ gives an additional transversely polarized bulk wave. The particle motion of the SAW lies in the sagittal plane (YZ plane) and $u_1$ and $u_3$ are nearly in phase quadrature. We have calculated the partial wave constants mentioned above for the case of YZ $LiNbO_3$. The values are given in Table 1 (values for n=4 are omitted as they do not contribute to the SAW in this case). They are normalized to $u_3(0)=1$. The magnitude squared values of the surface displacement amplitudes for YZ $LiNbO_3$ are given in [6]:

$$|u_j(0)|^2\omega \;/\; 4P = c_j \qquad j=1,3 \qquad (2)$$

with $c_1 = 3.16\cdot10^{-12}$ m$^3$ J$^{-1}$ and $c_3 = 6.86\cdot10^{-12}$ m$^3$ J$^{-1}$. $\omega$ is the frequency of the SAW and P is the power per unit width carried in the wave parallel to the propagation direction. In order to estimate $|u_j(0)|$, j=1,3 corresponding to a voltage $V_{in}$ applied to the IDT we assume that $|u_j(0)|$ increases linearly with $V_{in}$ (which might be false for large $V_{in}$ due to anharmonic effects). The input power $P_{in}$ is given by

$$P_{in} = V_{in}^2 G(\omega)/2 \qquad (3)$$

where $V_{in}$ is the peak applied voltage and $G(\omega)$ the frequency dependent input conductance.

This power is completely converted into acoustic power of the SAW if the number of finger pairs in the IDT is sufficiently large [7]. Then we may write

$$P = P_{in}/\,2a \qquad (4)$$

where a is the aperture of the IDT. This yields

$$|u_j(0)| = {}^1/_2 \left(c_j G(\omega)/\omega a\right)^{1/2} V_{in} \qquad (5)$$

For the next sections we define the abbreviations $a_l = |u_1(0)|$ and $a_t = |u_3(0)|$.

## 4. EXPERIMENTS

For our experiments we used YZ $LiNbO_3$ devices as shown in Figure 2 equipped with one IDT only. We had IDTs with different center frequencies (35 and 56 MHz) and substrates of different crystal quality at our disposal. The substrate was chosen such that no grain boundaries or ferroelectric domains impaired the wave excitation or propagation. In order to avoid strains and torsions the plate was glued onto the mounting at its right edge only. Both edges were than covered with adhesive acting as an acoustic absorber. The complete device was fixed on a goniometer.

Experiments have been performed at the white beam topography station at HASYLAB. The electron energy of the storage ring DORIS was 5 GeV with an average current of 17 mA. Two types of photographic material were used, single coated Kodak Industrex R film and Ilford L.4 nuclear emulsion plates. The exposure times were about 0.5 sec for the Kodak film and 2 - 3 times longer for the nuclear plate. The distance from the sample to the source is 34 m and the source size is about 2 mm vertically and 4 mm horizontally. The film was placed 5 to 20 cm behind the sample which was set for taking reflection topographs in the vertical diffraction plane because of the intrinsic polarization of the synchrotron radiation beam. The crystal was exposed to the white beam. Therefore one has to take into account the superposition of several harmonics in each Laue spot.

We concentrated on the (0k·0) reflections, k = 3, 6, ..., which represent net planes parallel to the YZ $LiNbO_3$ surface. This gives a symmetric Bragg case with the SAW amplitudes $a_t$ normal to the surface and $a_l$ parallel to the Z axis.

Figure 4 shows two reflection topographs from the same crystal. In topograph (a) no surface waves are excited. Each conducting wire gives rise to two shadows because they are illuminated by the incident and reflected beam simultaneously. The crystal has a dislocation density of about $10^4$ $cm^{-1}$ (or even higher - because of invisible dislocations) and no grain boundaries. The left side of the topograph appears much brighter and the edge is no straight line. This is the side where the crystal is fixed to the mounting. The distortions give a strong orientation contrast. The adhesive on the edges of the sample absorb photon intensity as can be seen on the right side of the topograph. The IDT is visible as a more strongly reflecting area because of the strains induced by the electrode structure.

In topograph (b) surface waves are excited at 35.4 MHz with 15 $V_{pp}$. On the left part of the topograph where the waves pass the strongly distorted surface the orientation contrast can be observed best. Depending on the



sense of the curvature of the netplanes the broader or narrower appears the spacing of the acoustic wavefronts. The oblique edge reflects surface waves despite of the adhesive. In addition the IDT excites spurious waves propagating along the X-axis. The fact that they are visible in the (03·0) reflection indicates a displacement component perpendicular to the surface.

The contrast formation of the SAW is demonstrated by the following experiment. A wire of 25 $\mu$m diameter was placed in front of the crystal at a height of about 1 mm inclined to the propagation direction of the SAW. The illumination condition was as illustrated in Figure 5 (a) so that the wire casts two shadows $s_1$ and $s_2$ onto the film. When comparing with the topograph in Figure 5 (b) $s_1$ has wavy but sharp borders. The valleys of the surface wave bring the reflected X-rays into focus, the hills defocalize, which explains the wavy shape. Shadow $s_2$, however, already occurs in the incident beam and its border lines give a diffuse image. This additional contrast arises from the penetrating wavefields which are deflected by the strain field of the SAW and emerge in area $s_2'$. This phenomenon has been investigated in case of homogeneous [8] and dislocation strain fields [9] and will be considered for this particular case in part II of this paper.

## 5. ORIENTATION CONTRAST FORMATION.

Usually the extinction length $\Delta_e$ which measures the thickness of the surface layer of the crystal which builds up the reflected beam is small compared to the acoustic wavelength $\Lambda$. For instance in the case of a 35 MHz IDT on YZ $LiNbO_3$ considered above we have approximately $\Lambda$ = 100 $\mu$m and for the 03·0 reflection with $\lambda$ = 0.18 nm the extinction length $\Delta_e$ = 6 $\mu$m. Even with the second order 06·0, ($\lambda$ = 0.09 nm) $\Delta_e$ = 22 $\mu$m is still a small fraction of the acoustic wavelength. In this case the curvature of the net planes due to a travelling Rayleigh wave does not change very much over the extinction length .

We then may approximate the Bragg reflection from a set of net planes parallel to the surface (symmetric Bragg case) by a simple mirror reflection from a corrugated surface. We neglect the changing lattice orientation inside the crystal which is seen by a penetrating wavefield. This effect can be separated from the surface reflected beam as demonstrated in Figure 5 and will be discussed in part II of this paper. The orientation contrast can be investigated by ray tracing calculations.

For this purpose we define a coordinate system with the xy-plane forming the undisturbed crystal surface. The xz-plane defines the scattering plane although small y components are allowed. This coordinate system differs

from the one used in the previous section by a rotation about the z-axis. Thus the acoustic wave propagation is not bound to the scattering plane. A source point is located at $R_s$ = (-L cosΘ, 0, L sinΘ), a distance L away from the crystal. The unit vector $\hat{s}_0$ = (cosΘ, 0, -sinΘ) points from the source to the origin. The angular deviation of a ray with respect to $\hat{s}_0$ is expressed by angles $\psi$ and $\varphi$, $\psi$ lying in the xz plane and $\varphi$ perpendicularly. Hence the ray direction is $s_0 = \hat{s}_0 + \Delta s_0$ with $\Delta s_0$= (-$\psi$ sinΘ, $\varphi$, -$\psi$ cosΘ). This ray hits the crystal surface at $r_c$ = (-L$\psi$/sinΘ, L$\varphi$, 0) (see Figure 6).

The Rayleigh wave is expressed in coordinates $r_o$ = (x,y) of the unperturbed crystal surface

$$r = (x - a_l \cos\beta \sin\Phi,\ y - a_l \sin\beta \sin\Phi,\ a_t \cos\Phi) \qquad (6)$$

with

$$\Phi = r_c \cdot K = LK(\varphi \sin\beta - \psi \cos\beta/\sin\Theta)$$

$\beta$ is the angle of the acoustic wave vector $K$ towards the x-axis.

The local surface normal $n$ is parallel to the vector $f = \partial r/\partial x \times \partial r/\partial y$ which is evaluated to

$$f = (a_t K \cos\beta \sin\Phi,\ a_t K \sin\beta \sin\Phi,\ 1 + a_l K \cos\Phi) \qquad (7)$$

and

$$f = |f| = \sqrt{1 + 2 a_l K \cos\Phi + K^2(a_l^2 \cos^2\Phi + a_t^2 \sin^2\Phi)}$$

Neglecting terms of second order in the amplitude we obtain

$$n = f/f = (a_t K \cos\beta \sin\Phi,\ a_t K \sin\beta \sin\Phi,\ 1) \qquad (8)$$

Obviously the longitudinal part of the Rayleigh wave can be omitted (which is no longer true with asymmetric reflections).

The "diffraction condition" $s_h = s_0 + h$ for unit vectors $s_0$ and $s_h$ yields

$$h^2 = -2\, s_0 \cdot h$$

$$h = -2\,(s_0 \cdot \hat{n})\, n$$

$$h = \begin{pmatrix} 2 a_t K \sin\Phi \sin\Theta \cos\beta \\ 2 a_t K \sin\Phi \sin\Theta \sin\beta \\ 2 \sin\Theta - 2 \cos\Theta(a_t K \sin\Phi \cos\beta - \psi) \end{pmatrix} \qquad (9)$$



Then we can determine the direction $s_h$ of the reflected ray

$$s_h = \begin{pmatrix} \cos\Theta - \psi \sin\Theta + 2 a_t K \sin\Phi \sin\Theta \cos\beta \\ \varphi + 2 a_t K \sin\Phi \sin\Theta \sin\beta \\ \sin\Theta + \psi \cos\Theta + 2 a_t K \sin\Phi \cos\Theta \cos\beta \end{pmatrix} \qquad (10)$$

The film is located a distance D away from the origin and is perpendicular to $\hat{s}_h$ = (cosΘ, 0, sinΘ) so that any point $r_f$ on the film fulfills the relation $r_f \cdot \hat{s}_h$ = D. The reflected ray with direction $s_h$ coming from $r_c$ hits the film at

$$r_f = r_c + t\, s_h \qquad (11)$$

where t = D + L$\psi$/tanΘ. The vector $r_f$ = (D cosΘ, 0, D sinΘ) lies in the film plane and leads to the film coordinates by setting

$$x_f = r_{f,y}$$

$$y_f = \sqrt{(r_{f,x} - D\cos\Theta)^2 + (r_{f,z} - D\sin\Theta)^2}$$

From eq. (12) and (13) we finally have

$$x_f = (L+D)\,\varphi + 2 D a_t K \sin\Phi \sin\Theta \sin\beta$$

$$y_f = (L+D)\,\psi - 2 D a_t K \sin\Phi \cos\beta \qquad (12)$$

Figure 7 shows some ray tracing maps for different crystal to film distances. The valleys of the surface wave focus the reflected waves at a certain distance, whereas the hills defocus resulting in a nonsinusoidal pattern with Λ-periodicity.

Lines of constant Φ which on the crystal surface form an angle $\beta$ towards the y axis are imaged on the film with an angle $\alpha$ towards the $x_f$ axis. These two angles are related by

$$\tan\alpha = \sin\Theta \tan\beta \qquad (13)$$

In order to calculate the local intensity we have to determine the area on the film illuminated by an incident ray bundle confined to the solid angle $d\psi d\varphi$. This area dF is obtained by

$$dF = \left|\partial(x_f,y_f)/\partial\psi \times \partial(x_f,y_f)/\partial\varphi\right| d\psi d\varphi \qquad (14)$$

$$= \left|(L+D)^2 + 2 D (L+D)\, a_t LK^2 \cos\Phi \,(\sin\Theta \sin^2\beta + \cos^2\beta/\sin\Theta)\right| d\psi d\varphi$$

With the area $dF_0 = (L+D)^2\, d\psi d\varphi$ corresponding to zero amplitude we find the intensity ratio

$$I/I_0 = dF_0/dF = \left[ 1 + 2\, D\, a_t\, K^2 \cos\Phi\, (\sin\Theta \sin^2\beta + \cos^2\beta/\sin\Theta)\, L/(L+D) \right]^{-1} \quad (15)$$

An analytical expression of the dependence of $I/I_0$ on the film coordinates rather than on the incidence parameters cannot be given as the reverse function of eq. (15) is multivalued beyond a certain distance $D_F$, the focal distance. For $D > D_F$ several contributions to the intensity must be added in certain areas (see Figure 7).

The focal distance is found by setting $\cos\Phi = -1$, $dF = 0$ and assuming $D \ll L$ which leads to

$$D_F = \sin\Theta \left[ 2\, a_t\, K^2\, (\sin^2\Theta \sin^2\beta + \cos^2\beta) \right]^{-1} \quad (16)$$

With $K = 2\pi/\Lambda$ we find for the extreme cases $\beta = 0°$ and $\beta = 90°$

$$D_F(\beta=0) = \Lambda^2 \sin\Theta \,/\, 8\pi^2\, a_t \quad (17)$$

$$D_F(\beta = 90°) = \Lambda^2 \,/\, 8\pi^2\, a_t \sin\Theta \quad (18)$$

With $\Theta = 37.5°$ and $\Lambda = 100\ \mu m$ a focal distance $D_F = 20$ cm is achieved by an amplitude as low as 0.38 nm ($\beta = 0$) or 1.04 nm ($\beta = 90°$), respectively.

For a given amplitude a wave travelling oblique to the scattering plane gives a weaker contrast than one with a parallel direction. This must be kept in mind when looking for scattered waves with different directions.

From eq. (5) we may calculate the amplitude $a_t$ for the 35 MHz IDT. With $\omega = 2\pi \cdot 35.4 \cdot 10^6\ s^{-1}$, a measured impedance $G(\omega) = 0.43$ mS and an IDT aperture $a = 1.57 \cdot 10^{-3}$ m we find $a_t/V_{in} = 0.092$ nm/V. Figure 8 shows for a fixed distance D and varying voltage $V_{in}$ the densitometer tracks of the SAW contrast observed under $\beta = 90°$. They are compared with theoretical curves obtained from eq. (15). In addition an extended source was taken into account by convolution with the geometrical image of the source produced on the film by reflection through one point on the crystal surface. The agreement is quite satisfactory.

By finding the focal distance $D_F$ and measuring the acoustic wavelength $\Lambda$ as well as the angles $\Theta$ and $\beta$, the acoustic amplitude $a_t$ can be determined in a straightforward manner. Unfortunately a source size of a few tenths of a millimeter is required for a precise determination of small amplitudes due to the increasing focal distance and the simultaneously increasing source image. A small pinhole close to the source is necessary in case of DORIS to perform these measurements with sufficient accuracy.



ACKNOWLEGDEMENTS.

We thank R. Veith and his coworkers of the Siemens AG, München, for the crystals, the possibility to use their facilities for preparation and fruitful discussions. One of us (H.C.) thanks DESY for financial support during his stay at Hamburg. This work was part of the project No. P 4937 of the Austrian Fond zur Förderung der wissenschaftlichen Forschung.

REFERENCES

1. C.-C. Glüer, W. Graeff, H. Möller, Proc. of the Intern. Conf. on X-Ray and VUV Synchrotron Radiation Instrumentation, Hamburg 1982, NIM 208, p. 701 - 704 (1983).

2. R.W. Whatmore, P.A. Goddard, B.K. Tanner, G.F. Clark, Nature 299, p. 44 - 46, (1982)

3. R.W. Whatmore, P.A. Goddard, B.K. Tanner, IEEE Ultrasonics Symposium Proc. Vol. 1, p. 363 - 367, (1982).

4. H.P. Feuerbaum, G. Eberharter, G. Tobolka, Scanning Electron Microscopy I, p. 503, (1980).

5. G. Eberharter, H.P. Feuerbaum, Appl. Phys. Lett. 37, p. 698 (1980).

6. 'Surface Acoustic Waves', A. A. Oliner (ed.), Topics in Applied Physics, Springer 1978.

7. N.H.C. Reilly, R.F. Milsom, M. Redwood, Electronic Lett. 9, p. 419 (1973).

8. U. Bonse, W. Graeff, Z. Naturforsch. 28a, p. 558 - 564 (1973).

9. U. Bonse, Z. Physik 177, p. 543 - 561 (1964).

FIGURE CAPTIONS

Figure 1. : Scheme of the stroboscopic technique. The SAW is synchronized to the incident photon pulses resulting in a standing wave pattern on the film.

Figure 2. : Photomicrograph of the 35 MHz YZ $LiNbO_3$ SAW device with a single interdigital transducer.

Figure 3. : X, Y, Z are rectangular crystal axis while $x_1$, $x_2$, $x_3$ are the coordinates of an orthogonal system defining SAW propagation in the Y cut, Z propagating case. $K$ is the acoustic wave vector.

Figure 4. : (a) Reflection topograph of the device shown in Figure 2. (Kodak R film) 24 mA, 0.2 s exposure time, $\theta = 25°$, (03·0) reflection. $h$ indicates the projection of the diffraction vector onto the film. (b) same as (a), but with SAW excitation.

Figure 5. : (a) Sketch how the two shadows in topograph (b) are formed. (b) Reflection topograph. (Kodak R film). 18 mA, 0.3 s exposure time, $\theta = 35°$, (03·0) reflection. The wire diameter was 25 $\mu$m.

Figure 6. : Coordinate systems used to simulate orientation contrast. Letters are explained in the text.



Figure 7. : Ray tracing maps with increasing film distance. (a) 78, (b) 156, (c) 234, and (d) 312 mm. Note the strong focusing in (b). Other parameters are $a_t = 0.5$ nm, $\Lambda = 100$ $\mu$m, $\beta = 30°$, $\theta = 30°$.

Figure 8. : Comparison of densitometer curves with theoretical curves. The input voltage has the following values: (a) $V_{in} = 2.5$ V, (b) $V_{in} = 5.0$ V, (c) $V_{in} = 7.5$ V. The distance D was fixed at 18 cm, the Bragg angle $\theta = 45°$ and $\beta = 90°$. The intensity curves calculated for a point source are convoluted with a source width of 3 mm corresponding to an image width of 16 $\mu$m.

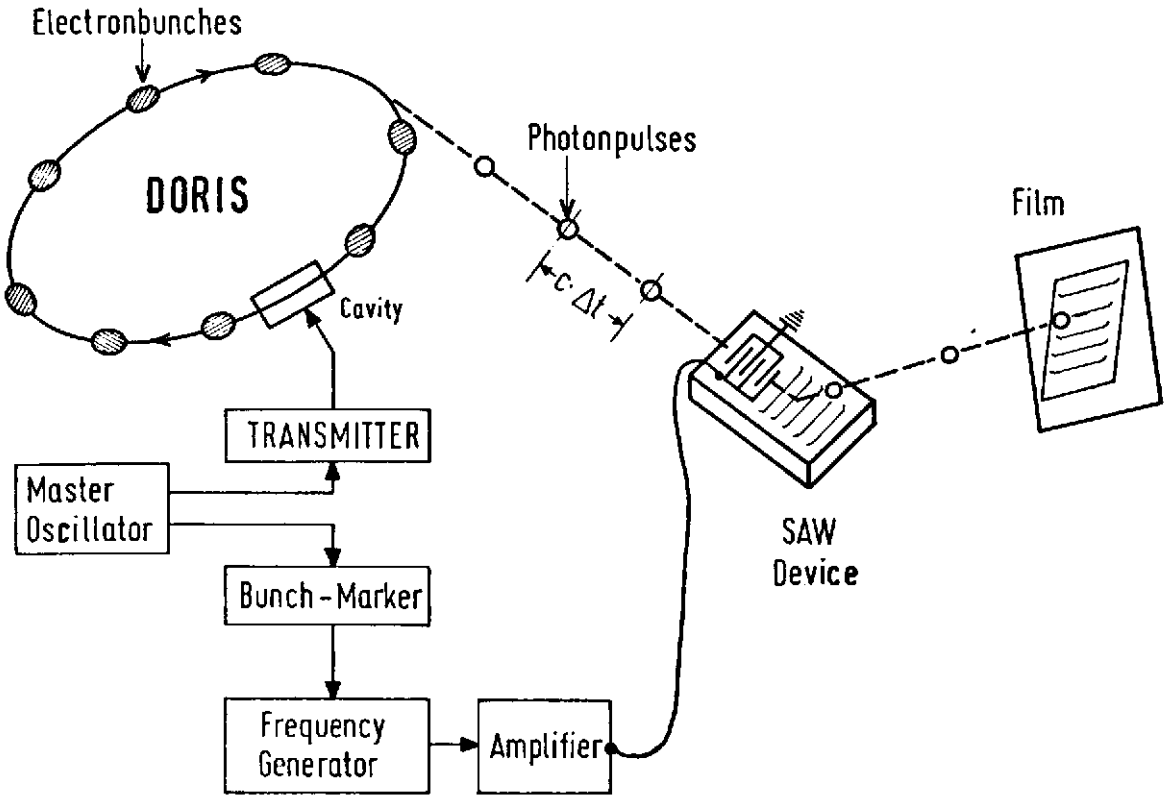


Fig. 1

| n | b(n) | j | $C(n)\alpha_j(n)$ |
|---|---|---|---|
| 1 | 0.3804 - i 1.0378 | 1 | -0.324 - i 0.497 |
| | | 2 | 0.0 |
| | | 3 | -0.078 + i 0.360 |
| | | 4 | -0.781 + i 0.211 |
| 2 | -0.3959 - i 0.7738 | 1 | 0.392 - i 0.269 |
| | | 2 | 0.0 |
| | | 3 | 0.098 - i 0.500 |
| | | 4 | 0.734 + i 0.480 |
| 3 | 0.0646 - i 0.1218 | 1 | -0.064 + i 0.088 |
| | | 2 | 0.0 |
| | | 3 | 0.980 + i 0.139 |
| | | 4 | 0.089 - i 0.139 |

Table 1. Partial wave constants for a SAW on YZ $LiNbO_3$, v = 3488 m/s

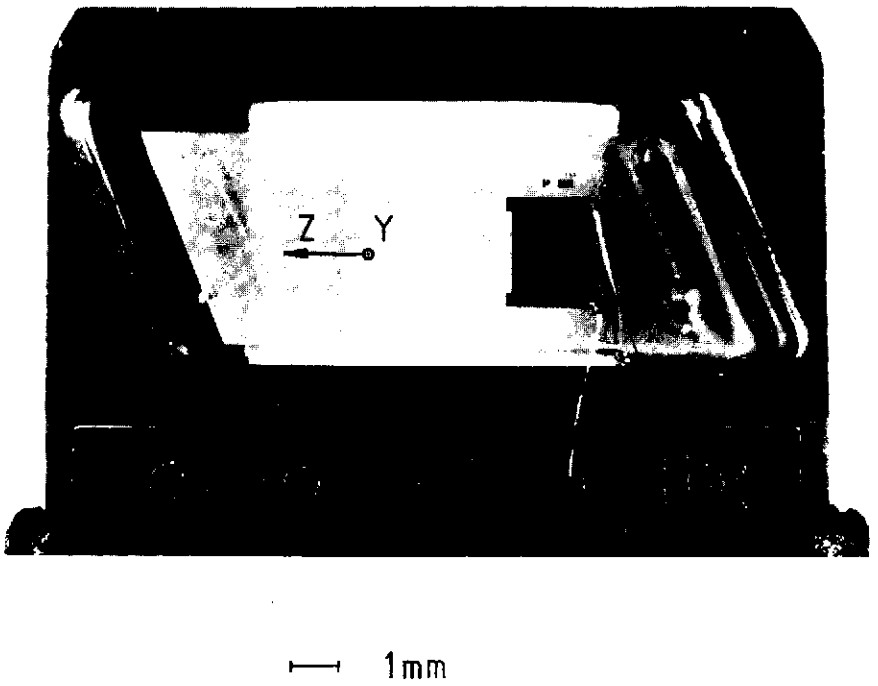


Fig. 2

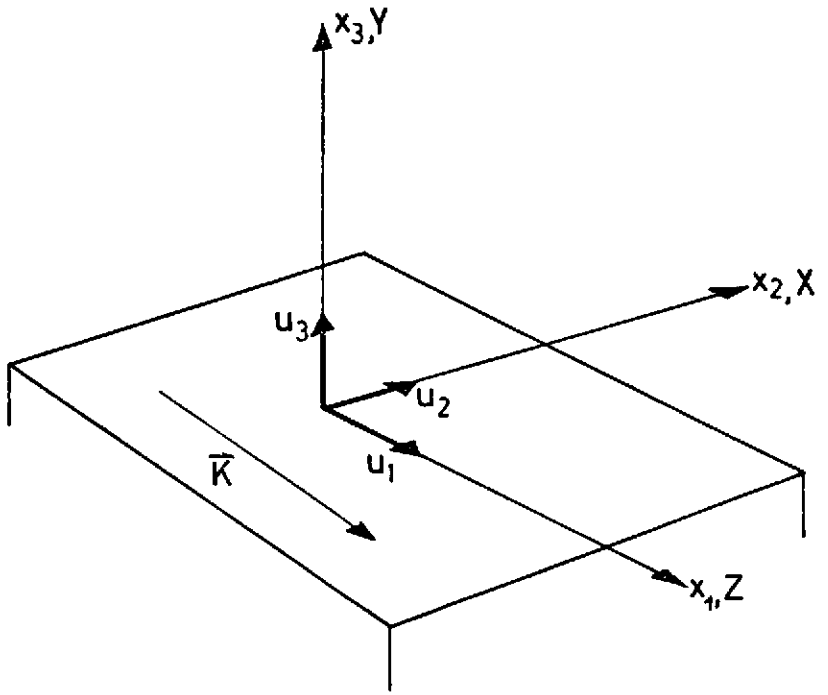


Fig. 3

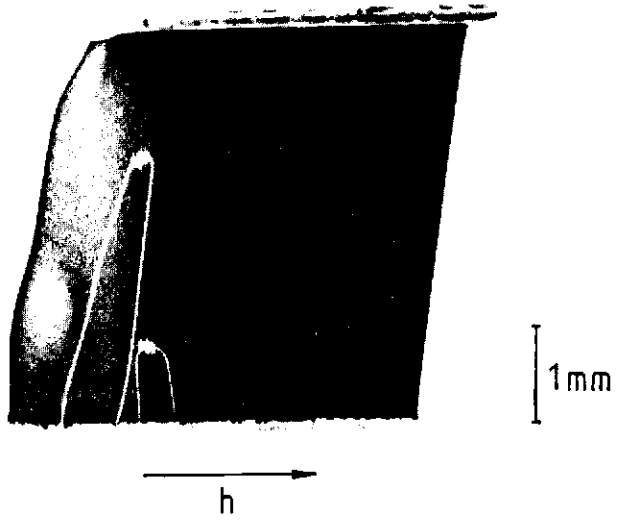


Fig. 4a

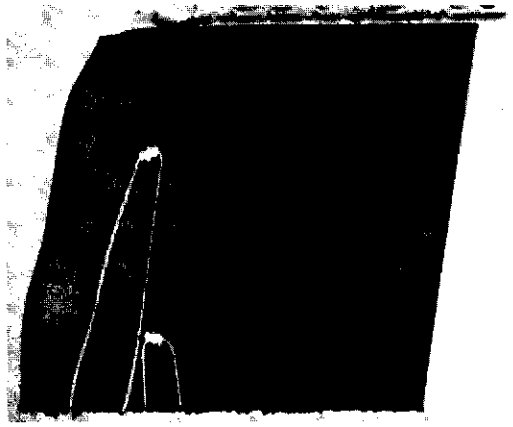

Fig. 4b

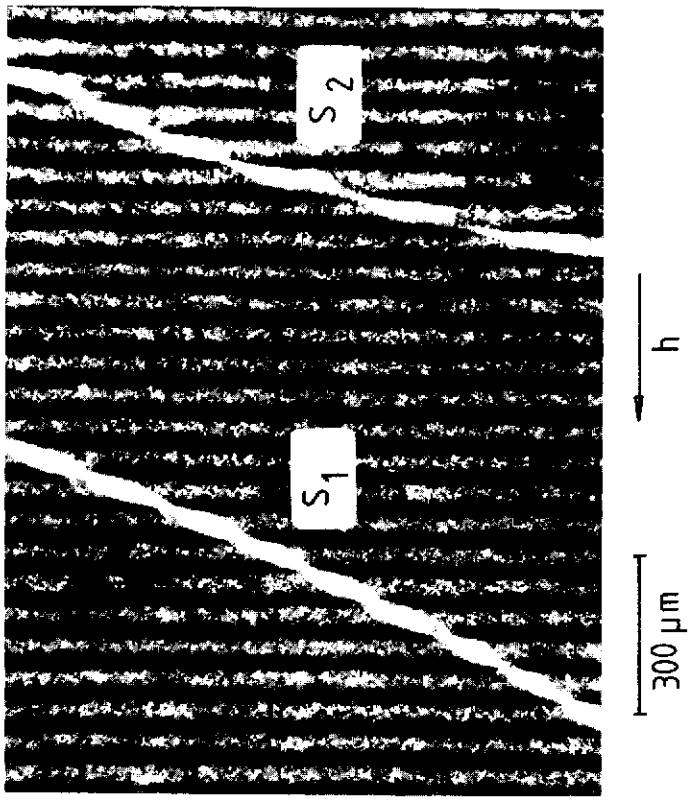


Fig. 5b

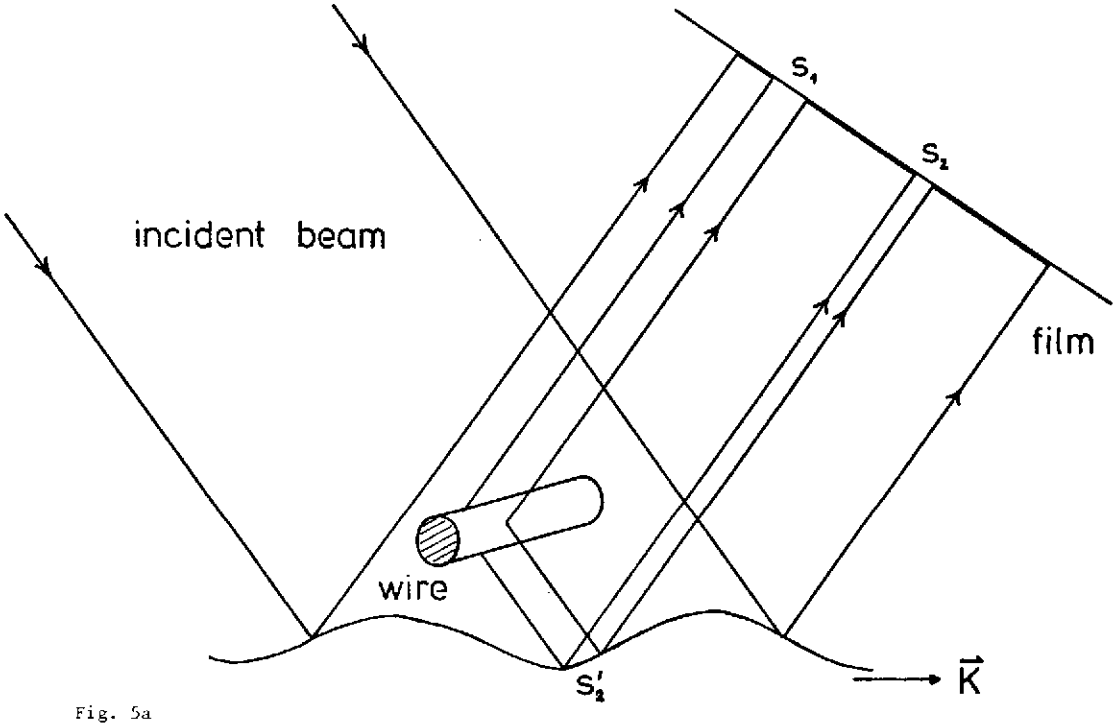


Fig. 5a

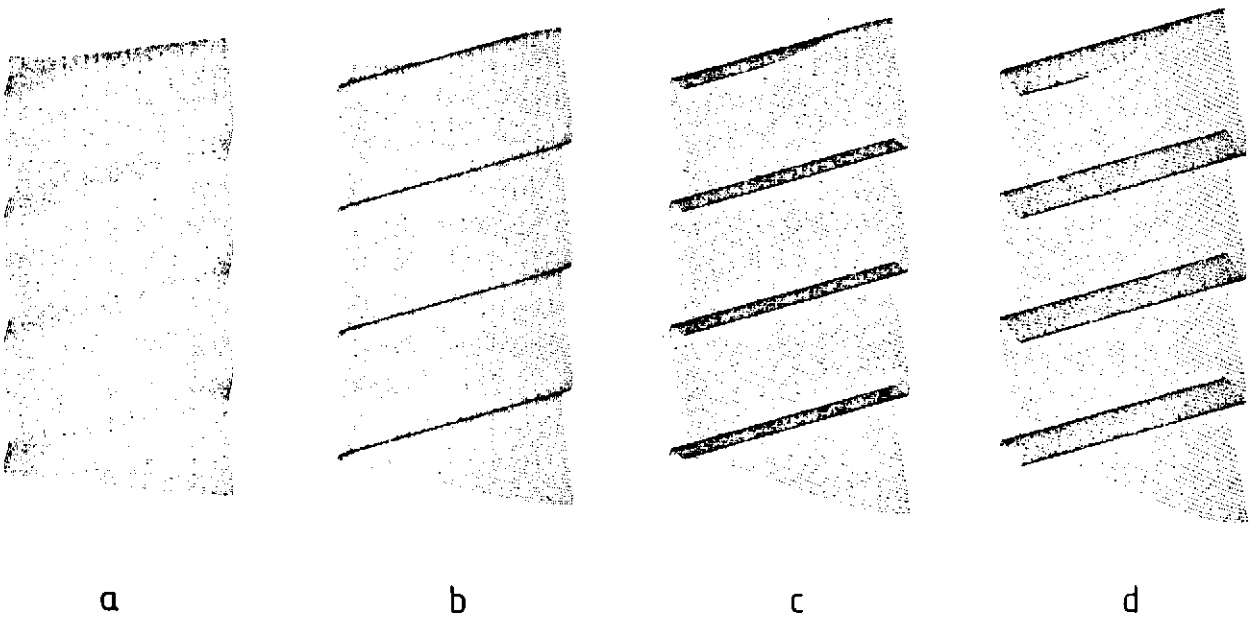


Fig. 7

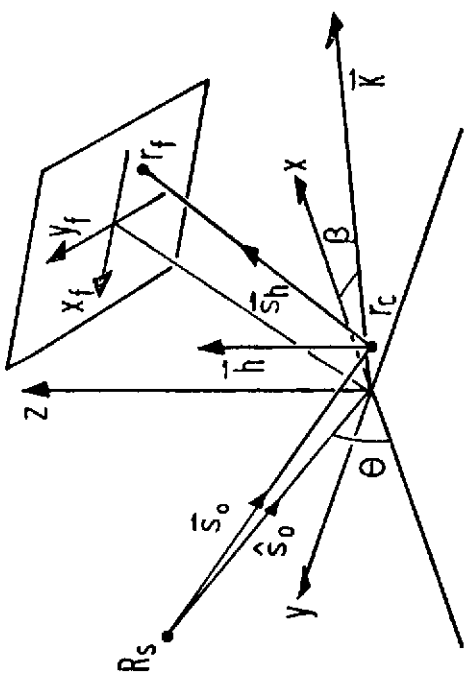


Fig. 6

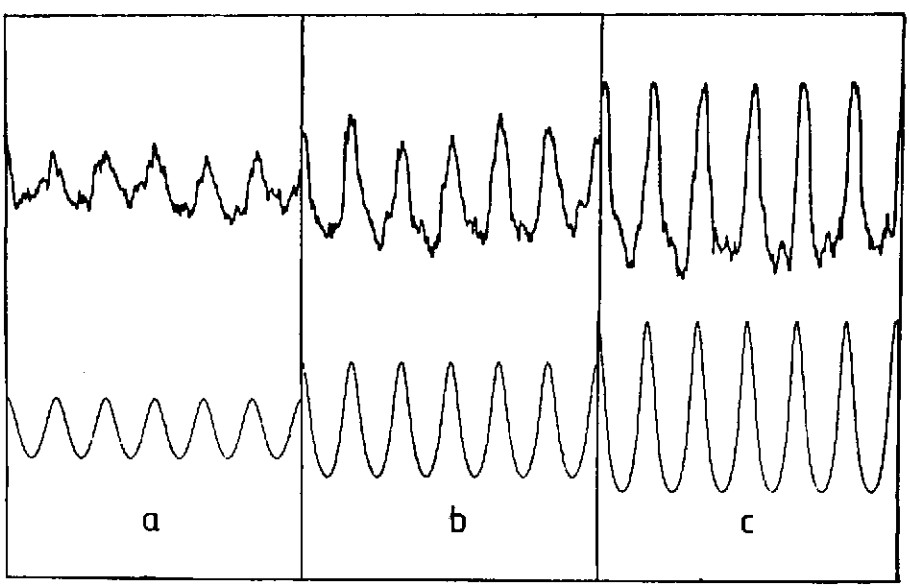


Fig. 8